scientific reports

Check for updates

OPEN

The role of mineralogical and textural complexity in the damage evolution of brittle rocks

Özge Dinç Göğüş[1]✉, Elif Avşar[2], Kayhan Develi[1] & Ayten Çalık[3]

In brittle rocks, deformation is characterized by the initiation and propagation of cracks at both microscale and mesoscale levels. This study explores how rock texture influences the evolution of cracking networks and progressive rock damage results under uniaxial compression. 3D discrete analyses were employed to identify the critical stresses of three different rock types. Thin sections were prepared from uniaxially loaded core samples at these stresses and crack patterns were captured under a polarizing microscope. The fractal box dimension method was used to quantitatively analyze the crack patterns for each rock type at each stress level. The novelty of this research is revealing the relationship between the development of microcrack patterns and textural properties such as mineral orientation/distribution, interlocking, crystal cleavage/hardness, and the groundmass. Results show that the cracking tendency varies with rock type at each critical stress level. Specifically, diabase exhibited the highest crack intensity, attributed to the interlocking of hard plagioclase and pyroxene crystals. Furthermore, the cleavages in pyroxenes make diabase particularly susceptible to cracking, especially when they are oriented parallel or semi-parallel to the applied load. These findings highlight that rock texture is a crucial factor influencing microcrack development, which should be considered in rock engineering applications.

Keywords Rock damage, Rock texture, Cracking, Discrete element method, Fractal dimension

Rock damage begins with micro-scale crack initiation and gradually progresses to macroscopic fractures at failure due to external stresses, such as tension and compression, applied to the rock. These stresses are often disturbed during engineering operations like excavation and tunneling. The fracturing mechanism and faulting that lead to rock failure occur in mediums such as intact rock, rock masses, and the Earth's crust. Since the 1920s, scholars (e.g[1–14]). have focused on the complexity of microscale deformations and distinguishing the primary fact unraveling the mechanism of microscale deformation underlying the subsequent mesoscale and macroscale damage in rocks reflects the importance of this phenomenon and the continuing interest in investigating it. Developments in microscope technology have enabled observational studies at the microscale, offering clear insights into the complex microcracking processes in rocks. For instance, the study of Howarth and Rowlands[15] has provided a solid basis for comprehending the effect of texture and mineralogical composition on rocks' strength and deformation properties. Similarly, Fahy and Guccione[16] and Shakoor and Bonelli[17] have made substantial contributions by revealing the impact of grain characteristics with mineralogical and textural properties on the strength of sandstones. In addition, the findings of some other studies[18–21] that investigate the effects of textural properties on the mechanical responses of rocks enrich our understanding of the multifaceted relationship between microscopic features and macroscopic behavior.

Martin[22], Eberhardt et al.[9,23], and Moradian et al.[24] have described critical stress levels that govern rock damage. Specifically, they identified crack initiation (σ_{ci}) and crack damage (σ_{cd}) stress thresholds which microcracks initiate first and propagate toward irreversible destruction. Finally, the ultimate stress (σ_{peak}) leads to macro fracture that signifies complete rock failure. Acoustic emission (AE) measurements have conventionally been employed in laboratories to assess crack density at various loading stages[25–33]. However, this method has some limitations, particularly in generating excessive noise in high-strength rocks or exhibiting low resolution, especially in heterogeneous rock formations[25,34]. In recent years, there has been a notable shift toward integrating X-ray tomography and digital image correlation techniques into laboratory tests to scrutinize crack progression with increasing axial stress at high resolutions[35–41]. However, applying these advanced techniques effectively requires both experience and significant financial investment.

[1]Geological Engineering Department, Istanbul Technical University, Istanbul 34469, Turkey. [2]Geological Engineering Department, Konya Technical University, Konya 42250, Turkey. [3]Geological Engineering Department, Canakkale Onsekiz Mart University, Canakkale 17100, Turkey. ✉email: dincgogus@itu.edu.tr

Some pioneering studies were published by Barton and Larsen[42], Anderson[43], Hirata[44], Barton[45], Berkowitz and Hadad[46] and Roy et al.[47] that used principles of fractal geometry for quantitative assessment of irregular and random patterns of rock fractures and fault systems. Examining the evolution of cracking patterns under different stress conditions, Zhao et al.[48] and Zhao[49] calculated the fractal dimension of microcracking initiation and propagation in marble slabs using SEM images and the box-counting method. Their findings revealed an increase in the fractal dimension with increasing stress levels. In more recent investigation by Ju et al.[50], a servo-controlled triaxial experimental method incorporating with a computerized tomography (CT) was employed to capture the images of coal samples. Employing the box-counting method to the CT images, they observed that the fractal dimension of crack networks initially decreased but exhibited an increase in later stages of loading. Similarly, Wang et al.[51] conducted X-ray CT scans on coal samples subjected to uniaxial and triaxial compression and suggested a linear correlation between three-dimensional box fractal dimensions and crack volume, crack speed, crack density, and inter-crack connections. Liu and Zhao[52] also used fractal dimension theory to explore the effect of impact durations on cracking mechanisms in different rock types under dynamic loads, considering mineralogical properties. Meanwhile, Lai et al.[53] scrutinized the influence of various loading rates on the fragmentation fractal dimension. However, these comprehensive studies, have yet to define cracking intensity or the evolution of the cracking process at different loading stages referring to the critical stresses. This collective body of research underscores the multifaceted nature of rock damage, incorporating both mineralogical considerations and fractal property.

This research conducts an examination of stress-induced cracking mechanisms from the microscale to the mesoscale in three different rock types under uniaxial compression loading. A novel approach is introduced to quantitively represent the evolution of rock damage, integrating experimental data with numerical modeling based on the discrete element method (DEM) while considering the mineralogical properties and fractal dimension. Critical stress levels (σ_{ci}, σ_{cd}, σ_{peak}) associated with microcracks were determined and the cracking patterns corresponding to these levels were correlated to the mineralogical composition and texture of diabase, ignimbrite, and marble. In detailed observations made on numerous thin sections extracted directionally from cores loaded up to the critical stresses: the impacts of the textural properties in terms of crystal hardness, cleavage in crystals, anisotropic distribution of minerals, interlocking, and groundmass on the evolution of cracking patterns were investigated.

Methodology

Sampling and laboratory tests

The laboratory testing program comprises mainly of the triaxial and uniaxial compressive strength and splitting tensile tests. The uniaxial and triaxial compression tests and tensile tests were conducted at the Rock Mechanics Laboratory of Dumlupınar University (Türkiye) and a stress-controlled press in the Concrete Laboratory at General Directorate of State Hydraulic Works (Türkiye) was used for the uniaxial compressive loading up the critical stresses. The thin sections were prepared and examined in laboratories at Istanbul Technical University. A total of 120 cylindrical core samples extracted from cubical rock boulders gathered from outcrops in the cities, of Bolu, Kayseri, and Afyon of Türkiye (Fig. 1a). The cores were prepared to be 54 mm in diameter with length-to-diameter ratios of 2.0 to 2.5 and sampling studies were performed in line with the procedures of ASTM D4543[54]. The uniaxial compressive strength tests were carried out following the ASTM D7012-14[54] method using a deformation control hydraulic press with a maximum load capacity of 1000 kN. The axial loads were arranged to increase continuously at constant strain rates of 0.005 mm/s, 0.004 mm/s, and 0.03 mm/s for diabase, ignimbrite, and marble samples, respectively until the complete failure of the rock samples was observed. Elasticity (tangential) modulus (E) and Poisson's ratio (u) values were calculated from the measurements recorded through linear variable differential transformers (LVDTs) that were implemented to the uniaxial compressive test device. In the triaxial compression strength tests (ASTM D7012-14[54]), a press with a maximum load capacity of 2000 kN and a Hoek cell capable of applying lateral pressure up to 420 bar were employed (Fig. 1b). The confining stresses σ_3 were increased as 2, 5 and 8 MPa and the peak stresses at the failure (σ_1 levels) were determined, afterward the failure envelopes were obtained from the σ_1-σ_3 data pairs. In the splitting tensile strength tests, disk-shaped samples with a thickness-to-diameter ratio (t/D) of 0.5 to 1.0 were used. Disk samples were loaded to failure within an average time of 25 to 30 s. The tensile strength of disk samples was determined following the ASTM D3967-16[54] testing procedures. Fracture patterns (failure planes) observed in the failed rock cores after the uniaxial compressive strength tests are presented in Fig. 1c.

Discrete modeling

The discrete element method (DEM) was employed for the numerical modeling analyses. DEM is a robust computational technique that simulates the interactions between discrete particles, allowing the simulation of complex rock behaviors. The primary objective of employing this method is to detect critical stress levels (σ_{ci}, σ_{cd}, σ_{peak}) associated with microcracking for each rock type. This is achieved through experimental simulations conducted on numerical models designed to accurately represent the mechanical behavior of real rocks. For this purpose, the 3D Yade open-source Discrete Element Method (DEM) software[55] was employed and the numerical models were established based on the bound particle model (BPM), initially proposed by Potyondy and Cundall[56] and subsequently refined by Scholtès and Donzé[57](Fig. 2a and b).

A rock model is generated with an assembly of particles that is arranged based on an interaction rate (γ_{int}) and a "constitutive contact law" expressed by the equation:

$$D_{eq} = \gamma_{int} * (R_a + R_b) \quad (1)$$

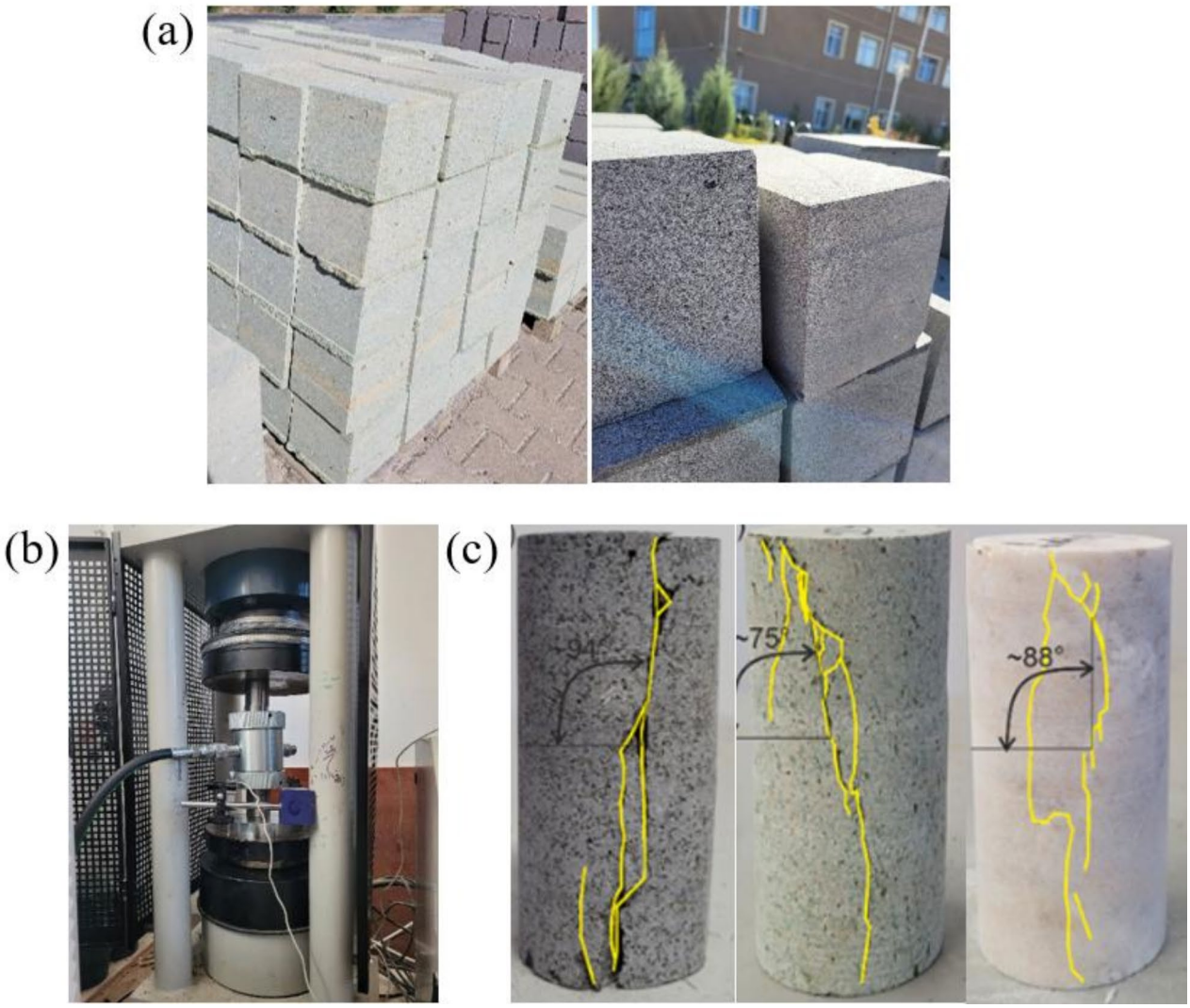

Fig. 1. Views from (**a**) cubical samples, (**b**) triaxial testing apparatus while testing, (**c**) macrocracks at the end of the UCS tests, and the angle of failure planes of (from left to right) diabase, ignimbrite, and marble.

where D_{eq} represents the primary distance between two particles, $\gamma_{int} \geq 1$ is the interaction rate, and R_a and R_b denote the radii of particles a and b, respectively. Here, $R_{max} / R_{min} = 2$, and $\gamma_{int} \leq 1.5$ in model samples. All rock models share the same particle size distribution in the discrete analysis. It is worth noting that particle size distribution has significantly affected the mechanical properties of rocks, so it has been extensively studied taking the heterogeneity into account in the numerical calculations (e.g[58–61]). Nevertheless, many of these studies have been focused on crystalline rock types, specifically granite and even though they are heterogeneous in terms of crystalline size, their textures are distributed homogeneously in the entire rock sample. Conversely, for instance, the ignimbrite used in this study has a heterogeneous texture, with a groundmass containing phenocrysts that vary in quantity from place to place. Therefore, to prevent complex model generation and to keep the numerical samples as much as simple for precisely detecting damage evolution, heterogeneity has not been considered in this study.

The average number of bonds per particle (N) is determined based on the degree of interlocking (γ_{int}) established at the initiation of the simulation. A lower γ_{int} value signifies reduced interlocking, representing a relatively weak rock mass. The incorporation of this feature by Scholtes and Donze[57] stemmed from the unsatisfactory UCS/UTS ratios reproduced by traditional BPM[56] and offers a relatively straightforward alternative to the advanced contact formulations advocated by Potyondy[62], Ding and Zhang[58]. Interaction forces between particles are categorized into normal force (F_n) and shear force (F_s). The normal force in the normal direction (F_n) is expressed as:

$$F_n = k_n * u_n \tag{2}$$

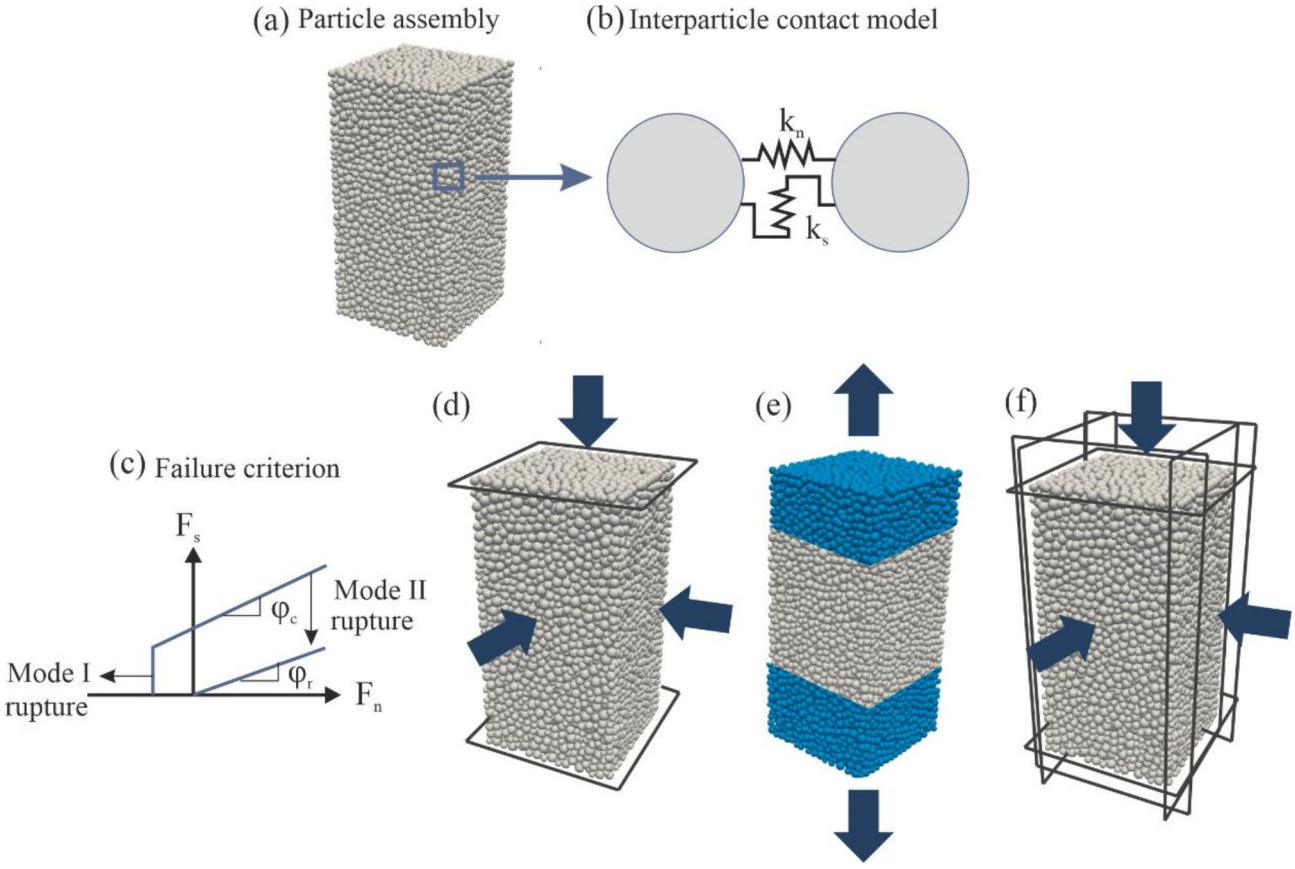

Fig. 2. (**a**) 3D DEM rock model sample generated based on BPM, (**b**) interparticle contact model with the normal and the shear stiffness, (**c**) interparticle failure criterion modified from Scholtès and Donzé[57], and configurations of (**d**) uniaxial compressive strength test, (**e**) uniaxial tensile strength test and (**f**) triaxial compressive strength test simulation.

$$k_n = 2Y\left[(R_a * R_b)/(R_a + R_b)\right] \tag{3}$$

where k_n is the normal stiffness value, a function of the equivalent elastic modulus (Y), and u_n is the normal relative displacement. Under compression, F_n increases without limit, reaching the threshold value $F_{n\max}=t\cdot A_{\text{int}}$ where t is the tensile strength. Upon surpassing $F_{n\max}$, the bond between particles breaks, resulting in a tensile crack (mode I).

The shear force (F_s) in the shear direction is calculated using:

$$F_s = F_s^{t-\Delta t} + k_s * \Delta u_s \tag{4}$$

where k_s is the shear stiffness, determined by $P\cdot k_n$, with P being a model constant in the range $0<P<1$. Δ_{us} represents the relative incremental displacement, and $F_{s\max}$, the maximum allowable shear force according to the Mohr-Coulomb criterion, is given by:

$$F_s^{max} = c * A_{int} + F_n * tan(\phi) \tag{5}$$

here c denotes the micro cohesion, and ϕ is the intergranular micro internal friction angle. When F_s surpasses $F_{s\max}$, shear failure occurs, leading to the development of a shear crack (mode II) at the location of the bond between particles. This detailed constitutive contact law governs the interactions and failure modes within the simulated rock model (Fig. 2c). Each micro-parameter (Y, P, t, c, φ, and N) delineated in the preceding description plays a pivotal role in the calibration process, influencing macro properties that govern the mechanical behavior of rocks. The interplay between these micro-parameters and their impact on macro-properties is elucidated below:

Y directly influences the Young (tangential) modulus (E) and the Poisson ratio (v). The macro-properties E and v are determined through simulations of uniaxial and triaxial compression as well as direct tensile tests.

The shear stiffness model constant (P) is calculated as the ratio of normal stiffness (k_n) to shear stiffness (k_s). It affects the calibration process by influencing the shear behavior of the rock material.

t controls the Ultimate Tensile Strength (UTS) value as it represents the tensile strength of the particles, while c influences the Uniaxial Compressive Strength (UCS) as it denotes the cohesion value of the particles.

ϕ is the micro-internal friction angle and is determined from triaxial compression test simulations by controlling the slope of the failure envelope of the rock.

N is determined prior to simulation commencement based on the ratio of UCS to UTS. It is directly related to the interaction ratio (γ_{int}) and is a crucial parameter in defining the particle interactions within the model.

During the modeling process, a non-viscous damping ratio of 0.4 was selected for quasi-static loading conditions, ensuring stability in all simulations. The numerical models had dimensions of $1 \times 2 \times 1$ (model unit) and comprised 10,000 discrete elements (DE), providing a high-resolution representation of the material. The simulations imitate standard laboratory tests, including uniaxial compression strength tests, direct tensile strength tests, and triaxial compression strength tests (True triaxial (TT) test setup).

Uniaxial Compression Strength Test Simulation (Fig. 2d):

Model samples were confined between two rigid frictionless plates, and a load was applied perpendicular to the sample axis.

Direct Tensile Strength Test Simulation (Fig. 2e):

Particles at the upper and lower boundaries of the samples moved in opposite directions along the vertical axis. To mitigate stress concentration at the boundaries, a recovery zone was established, prohibiting interparticle bond breakage within it. Consequently, the sample's complete failure could transpire distant from the boundaries, thereby safeguarding the intrinsic nature of the measured tensile strength.

Triaxial Compression Strength Test Simulation (True Triaxial Setup, Fig. 2f):

Samples were positioned between six rigid and frictionless plates, and once the desired lateral pressure was achieved, the upper and lower plates moved vertically at a constant unit deformation rate. The lateral stress applied in triaxial compression tests was controlled by the position of the side walls. The consistent movement speed was upheld throughout all experimental simulations, with a numerical loading speed of 0.025 m/s established based on preliminary sensitivity analysis findings. It's important to emphasize that this loading speed is purely numerical. To streamline modeling studies, it was assumed that all samples were devoid of discontinuities, and microcracks were initiated solely by the applied stresses. Calibrated microparameters for the model samples, representing the mechanical behavior of different rock types, are presented in Table 1.

In the 3D-DEM model samples, to determine the critical stresses (σ_{ci}, σ_{cd}, and σ_{peak}), 150,000 iteration steps have been performed in numerical modeling. When the simulation was completed, the data set in ".vtu" format for every 10,000 steps was imported into the Paraview software to determine the number and amount of cracks that developed until the relevant iteration steps. The total number of cracks in 15 separate levels and their localization regions where they concentrated in the model were detected. During the process, we determined the strain levels of the state of the cracks when they first emerged (σ_i) and progressed toward uncontrolled rock damage (σ_{cd}). Then, the stresses corresponding to these strain levels (iteration numbers) were recorded from the stress-strain curve as characteristic stresses (σ_i, σ_{cd}, and σ_{peak}).

Mineralogical examination

Disk-shaped samples with a thickness of 3 cm were carefully cut through the upper-three-centimeter portion of each rock sample (Fig. 3a). Thin sections extracted from these samples ascertained the core samples' undeformed original (or initial) texture. This method enabled the identification of primary cracks existing before laboratory loading, which were not taken into consideration in subsequent fractal analyses, as detailed in the following section. On the other hand, the core samples were subjected to uniaxial compression using a stress-controlled hydraulic press, gradually reaching the predetermined critical stress levels (Fig. 3b). Following that, the samples were cut both parallel and perpendicular to the loading direction. A total of 144 thin sections were prepared from the cut surfaces to examine under a polarized microscope (Fig. 3c).

In thin-section studies, a 4X magnification objective was utilized with a scaling parameter set to "mm" and clear images of the thin sections were captured. First, thin sections obtained from unloaded core samples were thoroughly examined using polarizing microscope (Fig. 4). Initial texture and inherent micro-cracks were detected, and conventional petrographic and mineralogical determinations were carried out through detailed thin section observations. The mineral names were abbreviated according to the definitions provided by Whitney and Evans[63]. Diabase primarily consists of plagioclase, pyroxene, and olivine (Fig. 4a). Euhedral to subhedral opaque minerals were observed as accessory minerals. Euhedral to subhedral plagioclase laths exhibit polysynthetic twinning. The rock displayed a typical ophitic texture, with high-relief, anhedral pyroxene crystals

Parameter	Diabase	Marble	Ignimbrite
Elastic Modulus Y (GPa)	13	12	10
Stiffness ratio P (-)	0.4	0.4	0.4
Interparticle tensile strength t (MPa)	11	7	9
Micro cohesion c (MPa)	77	56	74
Micro internal friction angle φ (°)	1	1	1
Coordination number N (-)	10	9	9

Table 1. Calibrated micro parameters of 3D-DEM models.

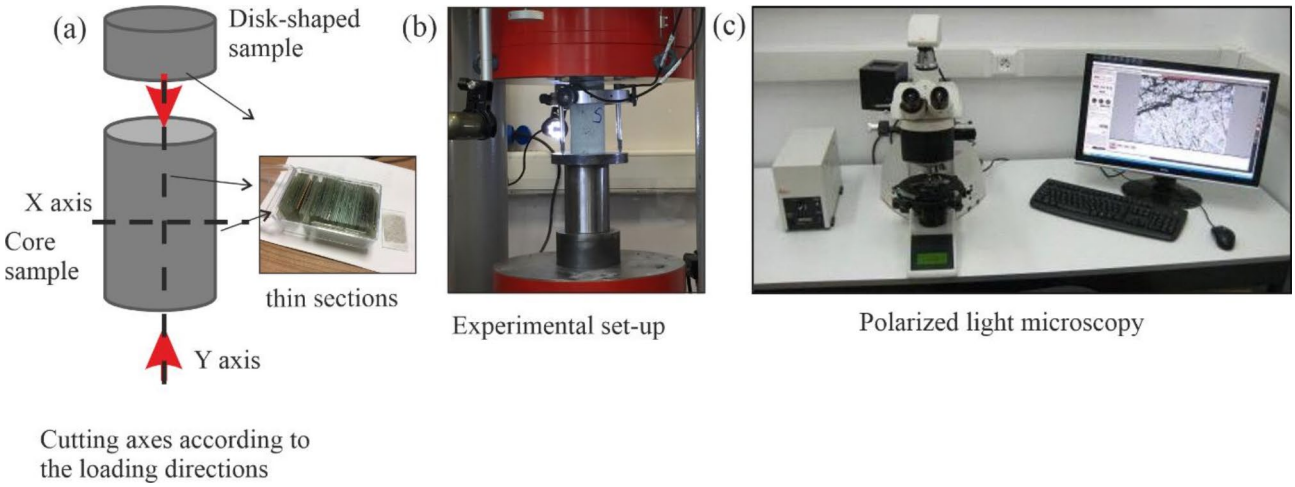

Fig. 3. (**a**) Cutting axes of disk-shaped and core samples concerning the loading direction, (**b**) stress-controlled loading set-up (**c**) polarized microscope set-up.

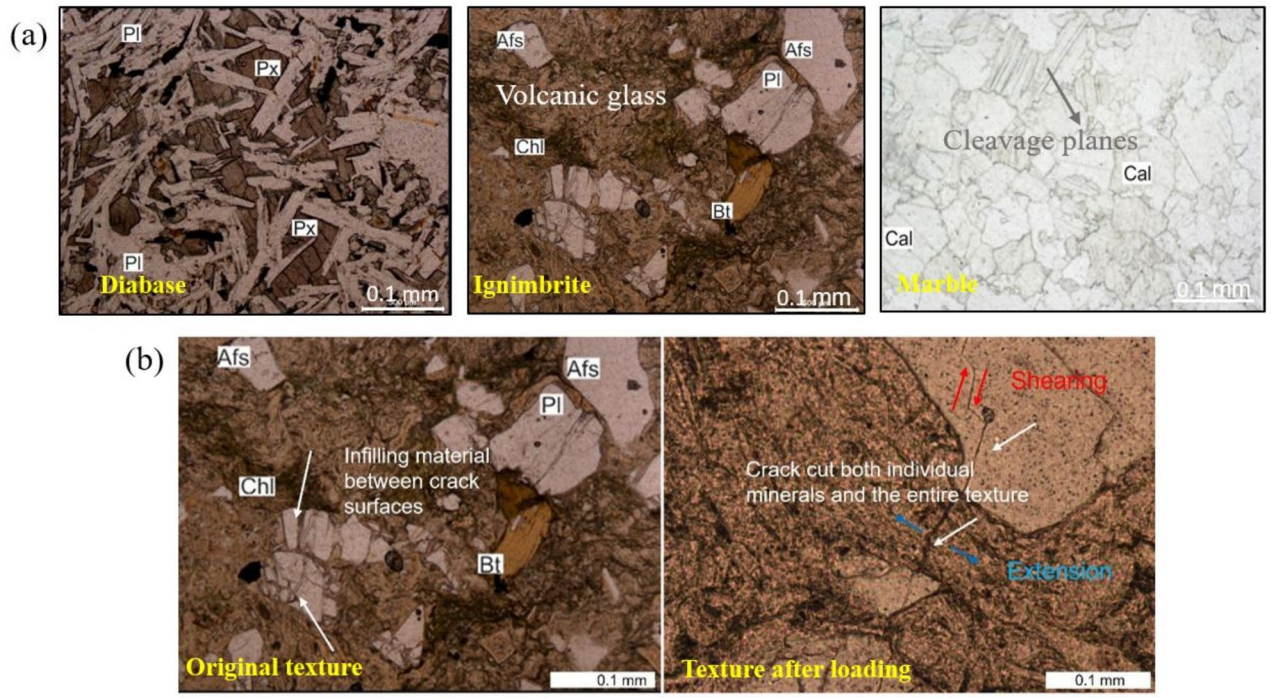

Fig. 4. (**a**) The primary texture and mineral composition of undeformed rock samples under a parallel-polarized light view (4X) Pl: Plagioclase, Px: Pyroxene, Afs: Alkali feldspar, Bt: Biotite, Chl: Chlorite, Cal: Calcite. (**b**) thin-section images of ignimbrite presenting inherent texture and mineral composition (left) and stress-induced texture after loading (right).

randomly enclosed within the plagioclase laths. Olivine crystals appeared as small, rounded grains, constituting a smaller proportion relative to other minerals. In ignimbrites, the groundmass is primarily composed of flattened vitric shards and crystal fragments. The phenocrysts in ignimbrites consist of alkali feldspar (sanidine), plagioclase, biotite, and a smaller amount of quartz (Fig. 4a). Broken phenocrysts may have formed due to the intensity of the eruption and mechanical breakdown during turbulent pyroclastic flow. Chloritization was also observed in the groundmass (volcanic glass). The mineral composition of marbles primarily consists of calcite minerals (see Fig. 4a). Anhedral calcite minerals are accompanied by small amounts of opaque minerals. Calcite crystals exhibit an anhedral form with cleaved, rhombohedral twins and are characterized by a granoblastic texture. Examining the primary texture of the rocks and the pre-existing cracks within this texture, it was noted that marble presented relatively smoother, crack-free, and more homogeneous surfaces compared to ignimbrite and diabase.

Crack patterns observed on thin section surfaces perpendicular to the loading direction predominantly are tensile cracks. In contrast, surfaces parallel to the loading direction tend to display a slightly higher occurrence of shear cracks compared to those in perpendicular sections. Nevertheless, tension cracks predominantly develop in all rocks along both directions. In this regard, the type of cracks has been identified considering both cracking tendencies with respect to the surface orientations and the properties such as pattern, shape, infilling, and aperture (separation) of the cracks examined through polarizing microscopy studies on thin sections. It has been observed that natural cracks were infilled, while the cracks induced by loading were identified as passing through both individual minerals and, in some areas, the entire texture. While the shear cracks have stepped paths and narrow or closed apertures, the tensile cracks are smoother and have more separated apertures (Fig. 4b).

Fractal box-counting method

The geometry of natural objects, spanning from the atomic scale to the vastness of the universe, plays a central role in the models aimed at comprehending the complexity of nature[64]. Unfortunately, the definition and quantification of the shape of many complex objects in nature are not adequately possible with the use of traditional Euclidean geometry. Introducing of the fundamentals of fractal theory by mathematician Mandelbrot[65] has provided a distinctive approach to quantify the geometry of natural objects that appear to be irregular and random with the concept of a very new dimension.

Discontinuities exist across a wide spectrum of scales, from microcracks to large faults, and this scale diversity, as well as three-dimensional distribution, geometry, and frequency, are mainly responsible for the overall mechanical behavior of fractured rock masses[45,66–68]. Therefore, in many previous studies, the fractal geometry has extensively been utilized for the quantification of in-situ discontinuities such as joints, fractures, and faults across various scales[42,44–47,69] as well as relatively in smaller scale samples induced by stresses in the laboratory conditions[49–51,53,70]. Fractal geometry provides a framework to quantify both size scaling and spatial clustering within fracture networks, capturing the full spectrum of complexity inherent in such systems. Note that, in fractal theory, higher fractal dimensions correspond to more complex networks of fractures/cracks.

The box-counting method is a well-known and reliable technique to calculate the fractal dimension values of crack networks as well as rough profiles[64,71,72]. The crack traces are covered by a grid of square boxes with a side length of r. Afterward, the number of square cells $N_{box\ (r),}$ surrounding any part of crack traces, is counted over the whole area of the thin section image. This process is run iteratively by decreasing the box sizes for a sequence of grids the relationship between $N_{box\ (r)}$ and r is given as;

$$D_B = \frac{logN_{box}}{\log\left(1/r\right)} \tag{6}$$

If the slope (β) of linear fit adjusted to the data in log N_{box} (r) vs. log r plot is read, this slope is related to the fractal dimension (D_B) through the following relationship:

$$D_B = -\beta \tag{7}$$

In this study, we applied the box-counting method using the Fraclac plugin in the open-source software ImageJ to find the fractal dimensions of 2D microcrack patterns digitized as 8-bit black and white binary images that have been captured from thin-sections. In Fraclac, the smallest box size was set to 2 pixels, and the largest box size was taken to be 30% of the binary image size. Here, "logN_{box}(r)- log r" graphs were obtained and the slopes (β) of the linear fits adjusted to the data on these plots were recorded as fractal dimension (-D_B). An example of "log N_{box} (r) vs. log r" graph derived from box-counting analysis is given in Fig. 5 with the coefficient of determination (R^2) of the relation.

Results

The results of the cracking evolution of diabase, ignimbrite, and marble, obtained through the combined methodologies described above, are presented as follows.

Based on the laboratory test results, the mean and standard deviation values of UCS, UTS, E, and υ of marble, ignimbrite, and diabase are presented with the results of the numerical model analysis in Table 2. The comparison of macro mechanical parameters obtained from laboratory experiments and 3D-DEM numerical simulations (Table 2) revealed a high level of compatibility between the two methods. Furthermore, the analysis of stress-strain behavior and Hoek-Brown failure envelopes, prominent failure criteria derived from triaxial compressive tests, showcased that the numerical models accurately represent the mechanical characteristics of actual rocks (Fig. 6). These findings confirm the reliability of determining critical stress levels for each rock type from discrete modeling.

In section "Methodology", the critical stresses detected for three rock types within the time interval of 150,000 iteration steps are as follows: for ignimbrite σ_{ci} = 25 MPa, σ_{cd} = 37 MPa, σ_{peak} = 47 MPa; for marble σ_{ci} = 21 MPa, σ_{cd} = 30 MPa, σ_{peak} = 38.5 MPa; and for diabase σ_{ci} = 38 MPa, σ_{cd} = 55 MPa, σ_{peak} = 75.5. These values indicate that in all rock types, the σ_{ci} stress level corresponds to approximately 50% of the UCS, while the σ_{cd} stress level corresponds to 75%. Normalizing σ_{cd} values with the UCS confirmed that these rocks exhibit characteristics of typical brittle rocks with low porosity[73]. Figure 7 illustrates the stress-strain behavior of all rocks under uniaxial loading conditions, depicting σ_{ci}, σ_{cd}, and σ_{peak} stress levels, as well as the number of iterations at these levels. All rock samples display linear-elastic behavior up to the σ_{ci} value during the early stages of loading (Fig. 7). With the incremental axial stress, microcracks accumulate significantly that causes disrupting the material's rigidity and deviation of the stress-strain curve from linearity. This deviation also signifies the σ_{cd} stress level of the respective

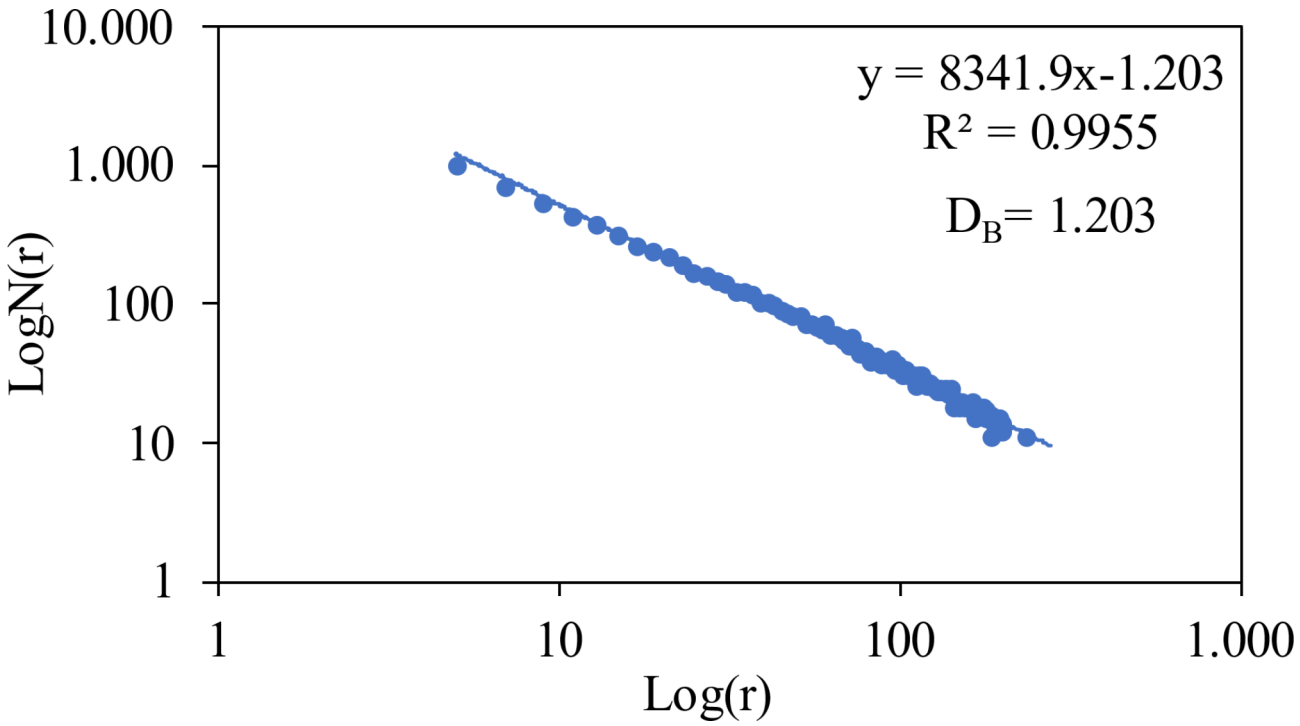

Fig. 5. A representative "log N_{box} (r) vs. log r" graph of marble obtained through the box-counting method for σ_{peak} stress level.

Parameter	Diabase		Ignimbrite		Marble	
	LAB	DEM	LAB	DEM	LAB	DEM
UCS(MPa)	72.57 ± 9.68	75.5	54.41 ± 7.67	47	41.46 ± 7.03	38.5
UTS(MPa)	9.14 ± 1.15	9.2	6.67 ± 0.78	6.53	4.85 ± 0.43	5.1
E (GPa)	10.88 ± 1.46	9.68	7.23 ± 1.07	6.4	8.32 ± 1.79	7.5
υ (-)	0.25	0.15	0.15	0.13	0.14	0.13

Table 2. Macro mechanical parameters of each rock type obtained from laboratory experiments (LAB) and 3D-DEM experimental simulations.

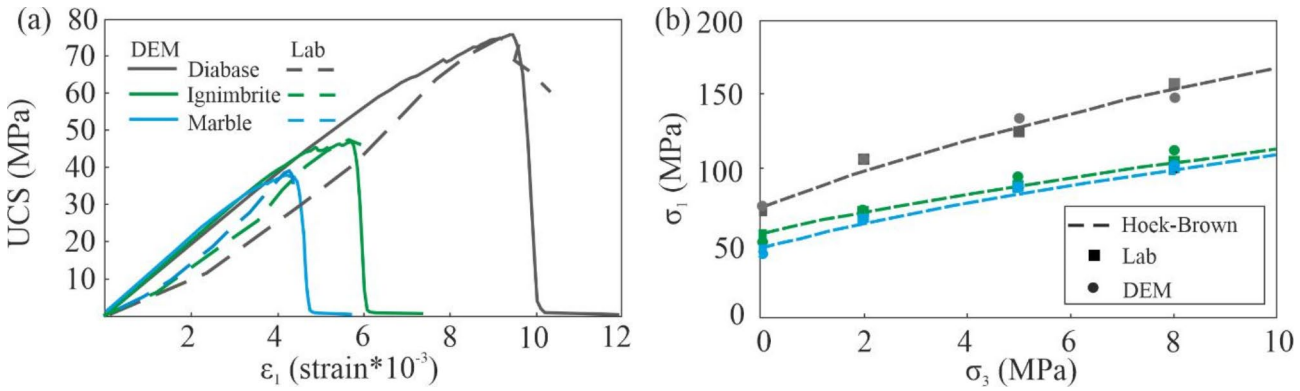

Fig. 6. Stress-strain responses under (**a**) uniaxial and (**b**) triaxial compressive loadings (Lab: Laboratory experiments, DEM: Laboratory test simulations based on discrete element method).

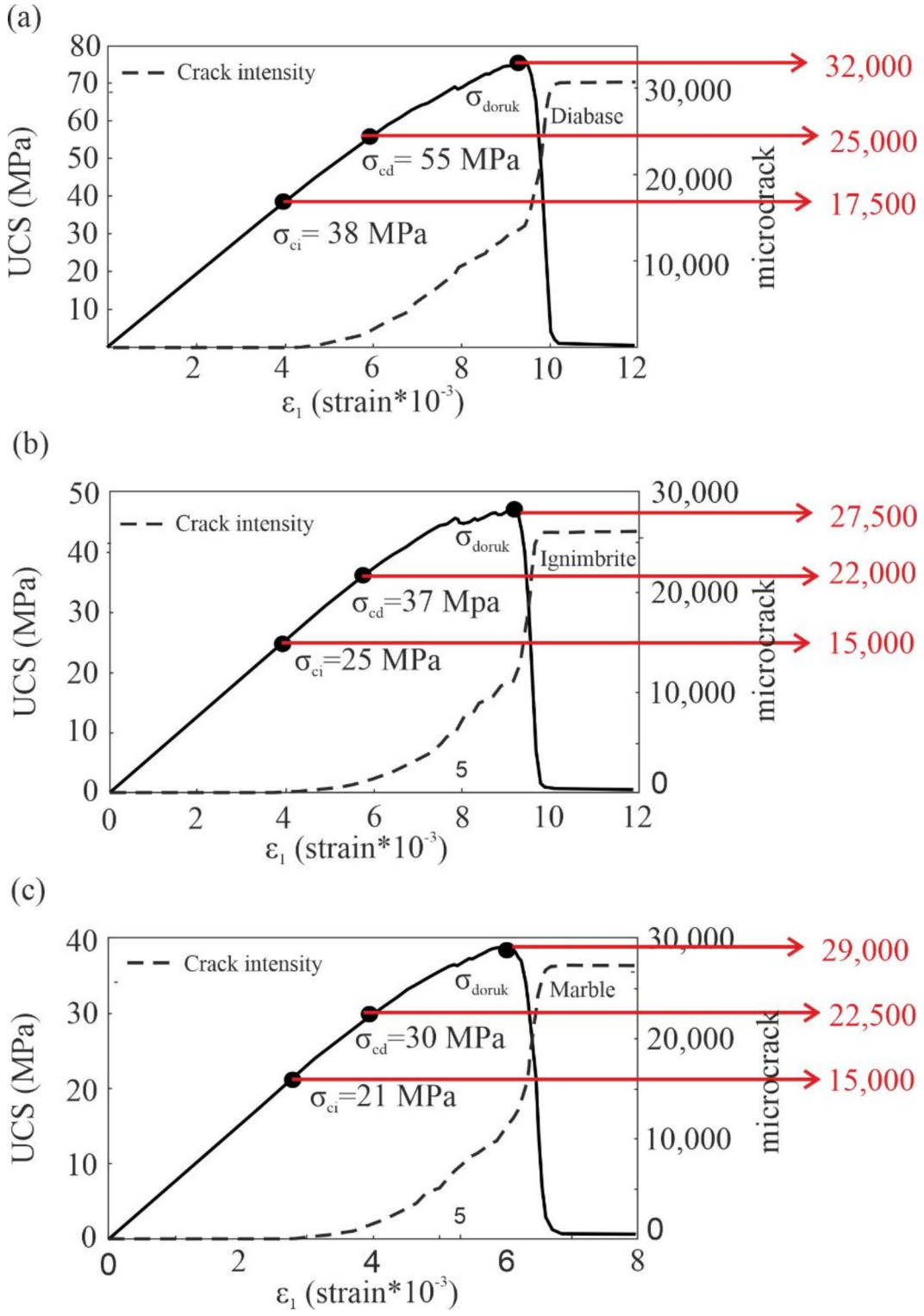

Fig. 7. Stress-strain responses of rock model samples under uniaxial compression (**a**) Diabase, (**b**) Ignimbrite, (**c**) Marble (red arrows: microcrack intensity relevant to iteration numbers at the critical stress levels).

rock, as experienced in previous studies[12,74–77]. Furthermore, 3D-DEM numerical model analyses revealed that microcracks in all rock types predominantly are tensile cracks (mode I), and only 1% of microcracks display shearing responses (mode II) (see Fig. 2c).

The results of box-counting analyses on microcrack patterns captured from thin-section images are summarized in Figs. 8 and 9 as well as D_B values at σ_{ci}, σ_{cd}, σ_{peak} stresses of diabase, ignimbrite, and marble. The findings indicated that the D_B values increase as the intensity of cracking increases accompanying incremental

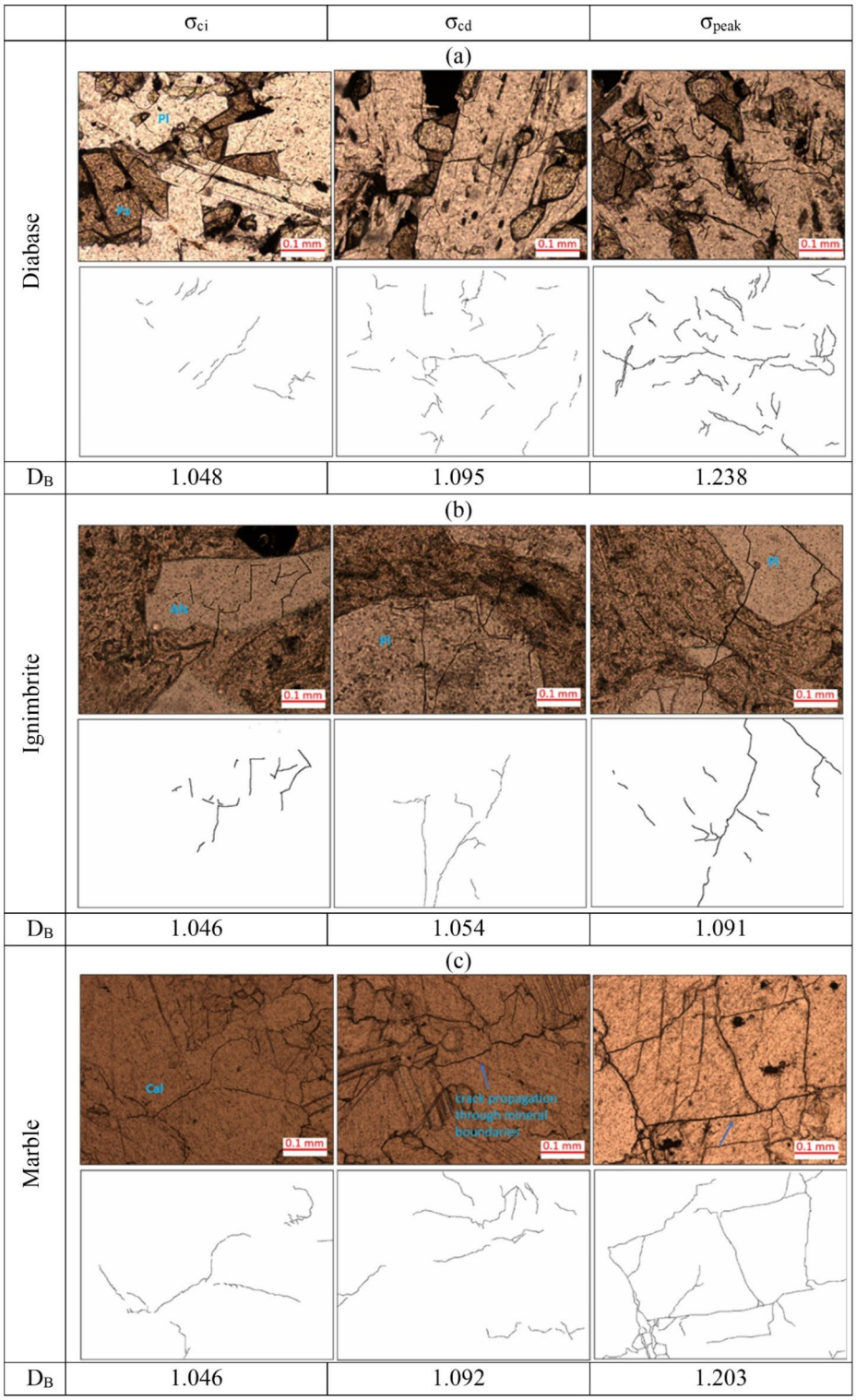

Fig. 8. Cracking evolution on the thin sections parallel to the loading direction (Y axis) and converted binary images of crack networks and D_B values at σ_{ci}, σ_{cd}, σ_{peak} stresses (**a**) diabase, (**b**) ignimbrite, (**c**) marble (Pl: Plagioclase, Px: Pyroxene, Cal: Calcite, Afs: Alkali feldspar).

critical stresses across all rock types. The D_B values belonging to thin sections parallel to the loading direction among all three rocks, diabase exhibited the highest crack intensity ($D_{B(Y\text{-}axis)}$: 1.048, 1.095, 1.248). Marble and ignimbrite shared the same $D_{B(Y\text{-}axis)}$ value of 1.046 at the crack initiation (σ_{ci}) stress level. However, upon reaching the crack damage threshold (σ_{cd}) stress level, marble exhibited a higher D_B value compared to ignimbrite ($D_{B(Y\text{-}axis)Marble}$:1.092; $D_{B(Y\text{-}axis)Ignimbrite}$: 1.054). With increasing stress, marble shows a significant decrease in

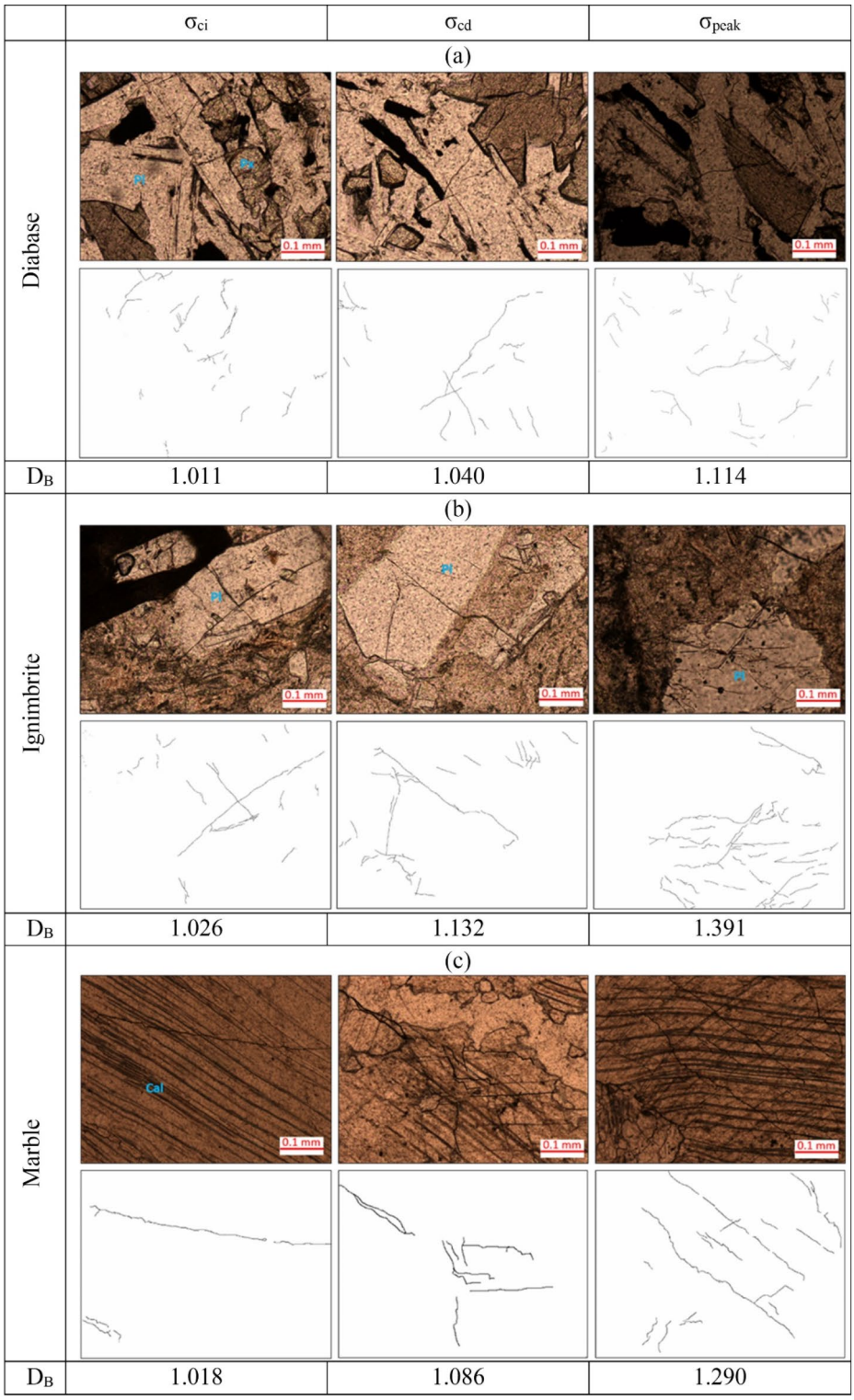

Fig. 9. Cracking evolution on the thin sections perpendicular to the loading direction (X axis) and converted binary images of crack networks and D_B values at σ_{ci}, σ_{cd}, σ_{peak} stresses (**a**) diabase, (**b**) ignimbrite, (**c**) marble (Pl: Plagioclase, Px: Pyroxene, Cal: Calcite).

strength compared to ignimbrite, creating a rock behavior more prone to cracking. On the other hand, cracking patterns emerged perpendicular to the loading direction, and ignimbrite exhibited the highest D_B value at all stress levels, starting from the σ_{ci} stress level ($D_{B(X\text{-}axis)ignimbrite}$: 1.026, 1.112, 1.391). Comparatively, marble has lower D_B values ($D_{B(X\text{-}axis)\ marble}$: 1.018, 1.086, 1.29), and diabase presented the lowest values ($D_{B(X\text{-}axis)\ diabase}$: 1.011, 1.040, 1.114).

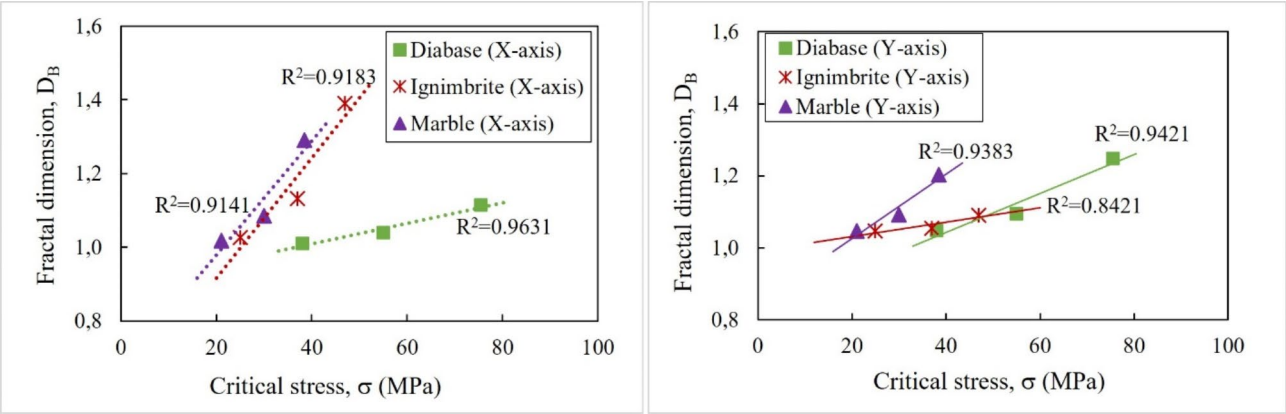

Fig. 10. Variation of the D_B of crack patterns at the critical stress levels along surfaces (**a**) perpendicular and (**b**) parallel to the loading direction.

Discussion

An increase in D_B values is observed with the intensification of microcrack patterns in rocks[49,51,52]. Since the D_B values is directly related to cracking processes, it is essential to consider the rocks' micro-composition and textures. In this context, we quantified the cracking process in three different rock types using fractal analysis, interpreting D_B values alongside our mineralogical examinations.

Considering the individual minerals in rocks, plagioclase, pyroxene, and alkali feldspars have similar hardness (≈5–6). Calcite and biotite, on the other hand, have lower hardness levels (≈2.5- 3). Biotites, with their layered structure, are more susceptible to deformation under pressure, leading to bending. Therefore, one can see that rocks comprising hard minerals tend to have higher strength. Nevertheless, our results show that despite the minerals' hardness, their distribution relative to each other within the entire rock is the primary factor influencing the damage process of a rock under stress. For instance, the texture formed by the significant interlocking of hard plagioclase and pyroxene crystals in diabase contributes to its rigidity and resistance to deformation. Thus, diabase exhibits both the highest strength and deformation parameters among the investigated rock types depending on its texture and crystallized hard minerals (see Table 2). On the other hand, the cleavage planes of hard pyroxenes make diabase the most susceptible to cracking among the rocks when these planes are oriented parallel or semi-parallel to the loading direction. This causes the diabase to exhibit the highest D_B value at all stress levels on the crack images along the Y-axis. A similar observation is noted in marbles. Although marble shares the same D_B value with ignimbrite at the initial stage of the loading (σ_{ci}) the twinning cleavages of calcite minerals (see Fig. 4a) being parallel to the loading direction led it to be more pronounced microcracking compared to ignimbrite with the increase in stress (σ_{cd} and σ_{peak}, respectively). This result may first suggest that the weakness planes of the crystals in ignimbrites are not parallel to the loading direction.

To achieve more accurate insights, we conducted a second series of fractal analyses, since the thin sections perpendicular to the loading direction also needed to be examined. The results of these analyses show that ignimbrite exhibited the highest D_B value at all stress levels, starting from the σ_{ci} stress level while marble has lower D_B values and diabase presented the lowest values. In the mineralogical examinations, it is monitored that the mineral orientations in ignimbrite exhibit more complex distributions, and they are surrounding by groundmass in significant amounts. In addition, some chloritization was observed in this fine-grained volcanic glass (see Fig. 4a). This suggests that the groundmass is the predominant factor on rock damage when the loading is oriented perpendicular to the core surface. This kind of content in ignimbrite also makes it to behave more ductile than the others. Verifying these findings, the angles concerning the loading direction of the mesoscale rock fractures measured in laboratory (at the post failure stage, σ_{peak}), one can see that diabase and marble fractured parallel-semi-parallel to the loading axis (approximately 94° and 88° from the x-axis, respectively), while ignimbrite exhibited a more oblique fracture pattern (approximately 75°) (see Fig. 1c). This alignment of mesoscale fractures is consistent with the microscale analysis results. In marble and diabase, cracks primarily developed parallel to the cleavages of crystals (calcite and pyroxene cleavages), while in ignimbrite, the clayey groundmass led to the microcracks development and caused the ductile behavior[21,52,78].

Figure 10 illustrates the graphical relationship between the critical stresses and the D_B, highlighting variations based on loading direction and rock type. Notably, diabase exhibits a distinct trend compared to ignimbrite and marble in Fig. 10a. Moreover, the D_B values of ignimbrite exhibit a narrower range of change along the surfaces that are parallel to the loading direction (Fig. 10b). Overall, the D_B values consistently demonstrate an increasing trend in both axes in three rock types.

Conclusions

In this comprehensive study, we employed the box-counting method for fractal calculations to assess the cracking regarding rock damage in three brittle rock types, diabase, ignimbrite, and marble at critical stress levels. Our combined approach consists of three methodologies to investigate the qualitative and quantitative relations between the strength and deformation properties and structural features of rocks.

1. The stress-strain responses of rocks obtained from 3D-DEM modeling are consistent with those determined by laboratory tests, confirming that critical stresses (σ_{ci}, σ_{cd}, and σ_{peak}) can be detected reliably from numerical models used in this study.
2. Identification of the mineralogical composition and textural structures of rocks shows that mineral hardness plays a critical role in rock strength at the early stages of the loading (σ_{ci}) whereas their distribution within the entire rock that forms the texture, controls the deformation behavior at incremental stress (σ_{cd} and σ_{peak}).
3. The composition and interlocking of crystals, presence of groundmass, and weakness planes (cleavages) are the most effective mineralogical properties on microcracking during the damage evolution of rocks.
4. Fractal analysis revealed that diabase exhibited the highest cracking intensity among the rock types, which is attributed to its complex texture formed by interlocking hard crystals. In addition to controlling rock strength, the planes of weakness within crystals and their alignment with the direction of applied stress influence crack susceptibility, as observed in both diabase and marble.
5. Even though ignimbrite exhibited higher compressive and tensile strength than marble, the presence of groundmass affects the rocks' behavior, presenting more cracking tendencies with increasing critical stress.
6. The fractal box-counting method can be used as an effective method to quantify progressive damage if the mineralogical observation is revealed accurately.

Data availability

This work is based on the data derived from numerical and laboratory experiments that are available through contacting the authors. The "numerical data" and the formulations used here can also be reproduced by following the equations in the text. Meanwhile, documentation and the details for the numerical code (called open source Yade DEM code) can be found online (at http://yade-dem.org and https://zenodo.org/record/34073#.Ygn-9d9BxPY). The data supporting this study's findings are available from the corresponding author upon request.

Received: 26 July 2024; Accepted: 13 November 2024
Published online: 19 November 2024

References

1. Griffith, A. A. The phenomena of rupture and flow in solids. *Phil Trans. Roy Soc. Ser. A*. **221**, 163–198 (1921).
2. Hoek, E. & Bieniawski, Z. T. Brittle rock fracture propagation in rock under compression. *Int. J. Fract. Mech.* **1** (3), 137–155 (1965).
3. Bieniawski, Z. T. Mechanism of brittle fracture of rock. Part I: theory of fracture process. *Int. J. Rock. Mech. Sci.* **4**, 395–430 (1967).
4. Lajtai, E. Z. Brittle fracture in compression. *Int. J. Fract.* **5**, 25–36 (1974).
5. Tapponnier, P. & Brace, W. F. Development of stress-induced microcracks in Westerly granite. *Int. J. Rock. Mech. Min. Sci. Geomech. Abstr*. **13** (4), 103–112 (1976).
6. Hoek, E. & Bieniawski, Z. T. Brittle fracture propagation in rock under compression. *Int. J. Fract.* **26**, 276–294 (1984).
7. Horii, H. & Nemat-Nasser, S. Brittle failure in compression: splitting, faulting, and brittle-ductile transition. *Philos. Trans. A Math. Phys. Eng. Sci.* 337–374 (1986). (1986).
8. Martin, C. D. & Chandler, N. A. The progressive fracture of Lac Du Bonnet granite. *Int. J. Rock. Mech. Min. Sci.* **31** (6), 643–659 (1994).
9. Eberhardt, E. D., Stead, B., Stimpson, R. S. & Read, D. Identifying crack initiation and propagation thresholds in brittle rock. *Can. Geotech. J.* **35**, 222–233 (1998).
10. Wong, L. N. & Einstein, H. H. Systematic evaluation of cracking behavior in specimens containing single flaws under uniaxial compression. *Int. J. Rock. Mech. Min. Sci.* **239**, 39–49 (2009).
11. Renard, F., Bernard, D., Desrues, J. J. & Ougier-Simonin A. 3D imaging of fracture propagation using synchrotron X-ray microtomography. *Earth Planet. Sci. Lett.* **286**, 285–291 (2009).
12. Dinç Göğüş, Ö. & Avşar, E. Stress levels of precursory strain localization subsequent to the crack damage threshold in brittle rock. *PloS One*. **17**, e0276214. https://doi.org/10.1371/journal.pone.0276214 (2022).
13. Dinç Göğüş, Ö., Avşar, E., Develi, K. & Çalık, A. Quantifying the rock damage intensity controlled by mineral compositions: Insights from fractal analyses. *Fractal Fract.* **7**, 383. https://doi.org/10.3390/fractalfract7050383 (2023).
14. Ou, J., Wang, E., Wang, X., Wang, B. & Zhu, G. Acoustic emission characteristics and damage evolution of different rocks under uniaxial compression conditions. *Sci. Rep.* **14**, 4179 (2024).
15. Howarth, D. F. & Rowlands, J. C. Development of an index to quantify rock texture for qualitative assessment of intact rock properties. *Geotech. Test. J.* **9**, 169–179 (1986).
16. Fahy, M. P. & Guccione, M. J. Estimating strength of sandstone using petrographic thin-section data. *Bull. Int. Assoc. Eng. Geol.* **16**, 467–485 (1979).
17. Shakoor, A. & Bonelli, R. E. Relationship between petrographic characteristics, engineering index properties, and mechanical properties of selected sandstones. *Bull. Assoc. Eng. Geol.* **28**, 55–71 (1991).
18. El Bied, A. J., Sulem, F. & Martineau, F. Microstructure of shear zones in Fontainebleau sandstone. *Int. J. Rock. Mech. Min.* **39**, 917–932 (2002).
19. Coggan, J. S., Stead, D., Howe, J. H. & Faulks, C. I. Mineralogical controls on the engineering behavior of hydrothermally altered granites under uniaxial compression. *Eng. Geol.* **89**, 89–102 (2013).
20. Öztürk, C. A., Nasuf, E. & Kahraman, S. A. Estimation of rock strength from quantitative assessment of rock texture. *J. South. Afr. Inst. Min. Andm*. **114**, 471–480 (2014).
21. Askaripour, M., Saeidi, A., Mercier-Langevin, P. & Rouleau, A. A. Review of relationship between texture characteristic and mechanical properties of rock. *Geotechnics* **2**, 262–296. https://doi.org/10.3390/geotechnics2010012 (2022).
22. Martin, C. D. *Strength of massive Lac du Bonnet granite around underground openings*. Ph.D. thesis, Department of Civil and Geological Engineering, University of Manitoba, Winnipeg (1993).
23. Eberhardt, E., Stead, D. & Stimpson, B. Quantifying progressive pre-peak brittle fracture damage in rock during uniaxial compression. *Int. J. Rock. Mech. Min. Sci.* **36**, 361–380 (1999).
24. Moradian, Z., Einstein, H. H. & Ballivy, G. Detection of cracking levels in brittle rocks by parametric analysis of the acoustic emission signals. *Rock. Mech. Rock. Eng.* **49**, 785–800 (2015).
25. Lockner, D. A., Byerlee, J. D., Kuksenko, V., Ponomarev, A. & Sidorin, A. Quasi-static fault growth and shear fracture energy in granite. *Nature* **350**, 39–42 (1991).
26. Lei, X. L., Kusunose, K., Nishizawa, O., Cho, A. & Satoh, T. On the spatio-temporal distribution of acoustic emissions in two granitic rocks under triaxial compression: The role of pre-existing cracks. *Geophys. Res. Lett.* **27** (13), 1997–2000 (2000).

27. Zang, A., Wagner, C., Stanchits, S., Janssen, C. & Dresen, G. Fracture process zone in granite. *J. Geophys. Res.* **105** (23), 651–661 (2000).
28. Baud, P., Klein, E. & Wong, T. Compaction localization in porous sandstones: Spatial evolution of damage and acoustic emission activity. *J. Struct. Geol.* **26**, 603–624 (2004).
29. Lei, X. Typical phases of pre-failure damage in granitic rocks under differential compression. *Fractal Analysis for Natural Hazards*, Geological Society, London, Special Publications 261, 11–29 (2006).
30. Zhao, X. G., Cai, M., Wang, J. & Ma, L. K. Damage stress and acoustic emission characteristics of the Beishan granite. *Int. J. Rock. Mech. Min. Sci.* **64**, 258–269 (2013).
31. Cheng, H., Yang, X., Zhang, Z., Li, W. & Ning, Z. Damage evaluation and precursor of sandstone under uniaxial compression: Insights from the strain-field heterogeneity. *PloS One*. **16**, e0262054 (2021).
32. Niu, Y. et al. Experimental study on thermal fatigue damage and failure mechanisms of basalt exposed to high-temperature treatments. *Fatigue Fract Eng Mater Struct*. 46(8), 10.1111/ffe.14052. (2023).
33. Niu, Y., Hu, Y. & Wang, J. Cracking characteristics and damage assessment of filled rocks using acoustic emission technology. *Int. J. Geomech.* **23** (4). https://doi.org/10.1061/IJGNAI.GMENG-8034 (2023).
34. Schubnel, A., Thompson, B. D., Fortin, J., Guéguen, Y. & Young, R. P. Fluid-induced rupture experiment on Fontainebleau sandstone: Premonitory activity, rupture propagation, and aftershocks. *Geophys. Res. Let.* **34**, L19307 (2007).
35. Besuelle, P., Desrues, J. & Raynau, S. Experimental characterisation of the localisation phenomenon inside a Vosges sandstone in a triaxial cell. *Int. J. Rock. Mech. Sci.* **37**, 1223–1237 (2000).
36. Louis, L., Wong, T. F. & Baud, P. Imaging strain localization by X-ray radiography and digital image correlation: Deformation bands in Rothbach sandstone. *J. Struc Geol.* **29**, 129–140 (2007).
37. Zhang, H., Huang, G., Song, H. & Kang, Y. Experimental characterization of strain localization in rock. *Geophys. J. Int.* **194**, 1554–1558 (2013).
38. Desrues, J. & Andò, E. Strain localisation in granular media. *C.R. Phys.* **16**, 26–36 (2015).
39. Ji, Y., Stephen, A. H., Baud, P. & Wong, T. F. Characterization of pore structure and strain localization in Majella limestone by X-ray computed tomography and digital image correlation. *Geophys. J. Int*. 700–719 (2015). (2015).
40. Renard, F. et al. Microscale characterization of rupture nucleation unravels precursors to faulting in rocks. *Earth Planet. Sci. Lett.* **476**, 69–78 (2017).
41. Shirole, D., Walton, G. & Hedayat, A. Experimental investigation of multi-scale strain-field heterogeneity in rocks. *Int. J. Rock. Mech. Min. Sci.* **127**, 104212. https://doi.org/10.1016/j.ijrmms.2020.104212 (2020).
42. Barton, C. C. & Larsen, E. Fractal geometry of two-dimensional fracture networks at Yucca Mountain, southwestern Nevada. *In Fundamentals of Rock Joints* (ed. Stephansson, O.), Centek, Björkliden, Sweden, (1985).
43. Anderson, T. L. Application of fractal geometry to damage development and brittle fracture in materials. *Scr. Metal.* **25**, 97–102 (1989).
44. Hirata, T. Fractal dimension of fault systems in Japan: Fractal structure in rock fracture geometry at various scales. *Pageoph* **131**, 157–170 (1998).
45. Barton, C. C. Fractal analysis of scaling and spatial clustering of fractures. In Fractals in the Earth Sciences (eds Barton, C. C. & La Pointe, P. R.) 141–178, Springer Science Business Media, New York, (1995).
46. Berkowitz, B. & Hadad, A. Fractal and multifractal measures of natural and synthetic fracture networks. *J. Geophys. Res.* **102**, 12, 205–212 (1997).
47. Roy, A., Perfect, E., Dunne, W. M. & McKay, L. D. Fractal characterization of fracture networks: An improved box-counting technique. *J. Geophys. Res.* **112**, B12201. https://doi.org/10.1029/2006JB004582 (2007).
48. Zhao, Y., Huang, J. & Wang, R. Real-time SEM observations of the microfracturing process in rock during a compression test. *Int. J. Rock. Mech. Min. Sci. Geomech. Abstr.* **30** (6), 43–652 (1993).
49. Zhao, Y. Crack pattern evolution and a fractal damage constitutive model for rock. *Int. J. Rock. Mech. Min. Sci.* **35** (3), 349–366 (1998).
50. Ju, Y. et al. Laboratory in situ CT observation of the evolution of 3D fracture networks in coal subjected to confining pressures and axial compressive loads: a novel approach. *Rock. Mech. Rock. Eng.* **51**, 3361–3375. https://doi.org/10.1007/s00603-018-1459-4 (2018).
51. Wang, D. et al. Quantitative analysis of fracture dynamic evolution in coal subjected to uniaxial and triaxial compression loads based on industrial CT and fractal theory. *J. Petrol. Sci. Eng.* **196**, 108051, 1–16. https://doi.org/10.1016/j.petrol.2020.108051 (2021).
52. Liu, K. & Zhao, J. Progressive damage behaviours of triaxially confined rocks under multiple dynamic loads. *Rock. Mech. Rock. Eng.* **54**, 3327–3358 (2021).
53. Lai, Y. et al. Fractal characteristics of rocks and mesoscopic fractures at different loading rates. *Geomechanics for Energy and the Environment* 100431 (2023). (2023).
54. ASTM. Annual Book of ASTM Standards-Soil and Rock, Building Stones, Section-4, Construction Vol. 04.08; ASTM Publications: Philadelphia, PA, USA. (2000).
55. Šmilauer, V. et al. *Yade Documentation* 2nd ed https://doi.org/10.5281/zenodo.34073. (2015). http://yade-dem.org
56. Potyondy, D. O. & Cundall, P. A. A bonded-particle model for rock. *Int. J. Rock. Mech. Min. Sci.* **41** (8), 1329–1364 (2004).
57. Scholtés, L. & Donzé, F. V. A DEM model for soft and hard rocks: Role of grain interlocking on strength. *J. Mech. Phys. Solids*. **61**, 352–369 (2013).
58. Ding, X. & Zhang, L. A. New contact model to improve the simulated ratio of unconfined compressive strength to tensile strength in bonded particle models. *Int. J. Rock. Mech. Min. Sci.* **69**, 111–119 (2014).
59. Peng, J., Wong, L. N. Y. & Teh, C. I. Influence of grain size heterogeneity on strength and microcracking behavior of crystalline rocks. *J. Geophys. Res. Solid Earth*. **122**, 1054–1073 (2017).
60. Hu, X. et al. Modeling damage evolution in heterogeneous granite using digital image-based grain-based model. *Rock. Mech. Rock. Eng.* **53**, 4925–4945 (2020).
61. Hu, X. et al. The effect of grain size heterogeneity on mechanical and microcracking behavior of pre-heated Lac Du Bonnet granite using a grain-based model. *Rock. Mech. Rock. Eng.* **56**, 5923–5954 (2023).
62. Potyondy, D. O. A flat-jointed bonded-particle material for hardrock. In: *Proceedings of the 46th US rock mechanics/geomechanics symposium*. American Rock Mechanics Association, Chicago, USA (2012).
63. Whitney, D. L. & Evans, B. W. Abbreviations for names of rock-forming minerals. *Am. Min.* **95**, 185–187 (2010).
64. Feder, J. & Fractals Plenum: New York, USA, (1998).
65. Mandelbrot, B. B. How long is the coast of Britain? Statistical self-similarity and Fractal Dimension. *Science* **155**, 636–638 (1967).
66. Witherspoon, P. A., Amick, C. H., Gale, J. E. & Iwai, K. Observations of a potential size effect in experimental determination of the hydraulic properties of fractures. *Water Resour. Res.* **15**, 1142–1146. https://doi.org/10.1029/WR015i005p01142 (1979).
67. Thorp, R. K., Watkins, B. J. & Ralph, W. E. Strength and permeability of an ultra-large specimen of granitic rock. In *Rock Mechanics Theory Experiment Practice*, Proceedings of the 24th US Rock Mechanics Symposium (C.C. Mathewson, ed.) (Texas A&M University Press), College Station (1983).
68. DeMarsily, G. Flow and transport in fractured rocks: connectivity and scale effect. *Int. Assoc. Hydrol. Mem.* **17**, 267–277 (1985).
69. Chiles, J. P. Fractal and geostatistical methods for modeling a fracture network. *Math. Geosci.* **20**, 631–654 (1998).

70. Zhang, Q. B. & Zhao, J. Quasi-static and dynamic fracture behaviour of rock materials: Phenomena and mechanisms. *Int. J. Fract.* **189**, 1–32 (2014).
71. Brown, S. R. & Scholz, C. H. Broad bandwidth study of the topography of natural rock surfaces. *J. Geophys. Res.* **90**, 575–582 (1985).
72. Power, W. L. & Tullis, T. E. Euclidean and fractal models for the description of rock surface roughness. *J. Geophys. Res.* **96**, 415–424 (1991).
73. Xue, L. et al. A study on Crack damage stress thresholds of different rock types based on Uniaxial Compression tests. *Rock. Mech. Rock. Eng.* **47**, 1183–1195 (2014).
74. Guo, S., Qi, S., Zou, Y. & Zheng, B. Numerical studies on the failure process of heterogeneous brittle rocks or rock-like materials under uniaxial compression. *Mater. (Basel).* **10**, 378. https://doi.org/10.3390/ma10040378 (2017).
75. Dinc, Ö. & Scholtès, L. Discrete analysis of damage and shear banding in argillaceous rocks. *Rock. Mech. Rock. Eng.* **51**, 1521–1538 (2018).
76. Li, X. F. et al. Investigating the crack initiation and propagation mechanism in brittle rocks using grain-based finite-discrete element method. *Int. J. Rock. Mech. Min. Sci.* **127**, 104219 (2020).
77. Zhang, L., Scholtès, L. & Donzé, F. V. Discrete element modeling of permeability evolution during Progressive failure of a low-permeable Rock under Triaxial Compression. *Rock. Mech. Rock. Eng.* **54**, 6351–6372 (2021).
78. Ersoy, A. & Waller, M. D. Textural characterization of rocks. *Eng. Geol.* **39**, 123–136 (1995).

Acknowledgements

This research was financially supported by the Scientific and Technological Research Council of Turkey (TÜBİTAK) under Project Grant 121Y031. We gratefully acknowledge Prof. Kamil Kayabalı and the Rock Mechanics Laboratory at Ankara University for providing the rock samples used in this paper.

Author contributions

Özge Dinç Göğüş: Conceptualization, Methodology, Software, Validation, Formal analysis, Investigation, Visualization, Writing- Original draft preparation. Elif Avşar: Software, Investigation, Methodology, Visualization, Writing- Original draft preparation. Kayhan Develi: Formal analysis, Investigation, Writing- Reviewing and Editing. Ayten Çalık: Investigation, Visualization, Writing.

Declarations

Competing interests

The authors declare no competing interests.

Additional information

Correspondence and requests for materials should be addressed to Ö.D.G.

Reprints and permissions information is available at www.nature.com/reprints.

Publisher's note Springer Nature remains neutral with regard to jurisdictional claims in published maps and institutional affiliations.